

Inverse design of Mie resonators with minimal backscattering

Vladimir Igoshin, Alexey Kokhanovskiy, and Mihail Petrov

School of Physics and Engineering, ITMO University

(*Electronic mail: m.petrov@metalab.ifmo.ru)

(Dated: 11 September 2024)

Manipulation and engineering of light scattering by resonant nanostructures is one of the central problems in optics and photonics. In this work, we theoretically study the effect of suppressed back-scattering of dielectric nanoantenna. We employed covariance matrix adaptation evolution strategy to identify the geometries of circular dielectric structures with minimized backward scattering cross section. Zero back-scattering is achieved due to generalized Kerker effect and multipole cancellation condition. We found a set of geometries and shapes of the nanoantenna having back-scattering intensity close to zero. With help of clustering algorithms, all the found geometries fall separated into several groups according to their multipolar content. While the optical properties of scatterers in each group were similar due to similar multipolar content, their shapes can be significantly different which stresses the ambiguity of free-form optimization problem. We believe that the obtained results and found possible classes on generalized Kerker nanoantenna can help in designing nanophotonic structures such as antireflective metasurfaces.

Modern nanophotonics is advancing towards more complex systems with an increasing number of controlling parameters^{1,2}. For instance, changing the shape of metaatoms, which are the essential building blocks of optical metastructure, from highly symmetric primitives such as cylinders and spheres to more sophisticated shapes immediately expands their optical functionality³⁻⁸. However, increasing the complexity of metaatoms immediately results in a lack of analytical solutions and inevitable increase of computational complexity⁹. Addressing this problem, development of methods for inverse design of metaatoms and metastructures with given optical properties and functionality becomes one of the topical fields of research¹⁰⁻¹³.

Deep learning algorithms, particularly artificial neural networks, are recognized as universal approximators and are widely used for design tasks, having already shown remarkable results^{14,15}. These algorithms were applied to optimize optical properties of metaatoms such as core-shell structures^{12,16}, nanoparticle arrays¹⁵, thermal emitters¹⁷, including optimization the geometry of free form objects¹⁸⁻²⁰. Despite their success, there remains significant controversies and unanswered questions regarding the feasibility of using machine learning algorithms for design tasks²¹. One of the major challenges is obtaining a statistically significant dataset that adequately represents the problem. Alternative approach to inverse design of nanophotonic systems is based on evolutionary optimization methods²²⁻²⁴. In contrast to the machine learning algorithms, they do not require preliminary generation of a dataset. Moreover, the advanced algorithms based on covariance matrix adaptation evolution strategy (CMA-ES)²⁵ do not require calculation of approximate gradients of the objective function either and can be used for non-smooth, non-continuous, and nonlinear fitness functions²⁶.

In this work, we tackle the problem of finding optimal geometry of cylindrically symmetric dielectric scatterers with minimal backscattering cross-section. The effect of suppressed backscattering in nanophotonics is associated with Kerker effect^{27,28} and finds its applications in manipulating of nanoantenna directivity^{29,30} and designing anti-reflecting coating^{31,32}. Suppression of backscattering has been already

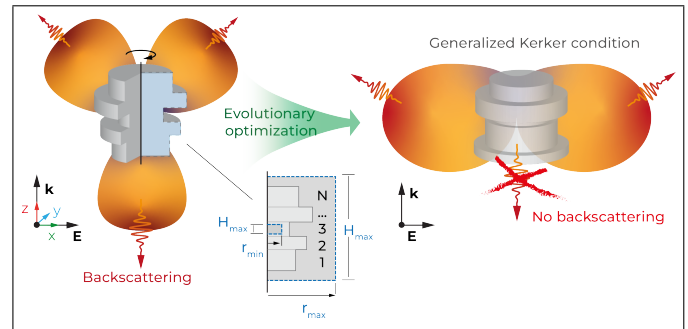


FIG. 1. The main idea of this work is shown: evolutionary optimization algorithm finds the geometry of dielectric cylindrical nanoantenna consisted of N section having minimal scattering intensity on in the backward direction. The inset shows the geometry of the considered system before the revolution operation. The red dashed lines show the constraints: minimal and maximal size of the structure.

demonstrated in dielectric scatterers with basic primitive shapes such as dielectric conical^{5,6} and spheroidal particles³³, dielectric cubes and pyramids⁵. Limited number of parameters of these geometries primitives can be manually optimized, while address this problem from the free-form perspective.

Here, we utilize CMA-ES evolutionary optimization algorithm to find the geometry of high refractive index dielectric scatterer composed of N sections, coaxially stacked cylinders, as shown in Fig. 1. By increasing the number of sections and, thus, the number of free parameters, we approach to the free-form geometry of the scatterer. We assume that the scatterers are placed in vacuum surrounding. The refractive index of each cylinder is fixed to $n = 4$ which is close to many dielectric materials such as semiconductors in the visible and infrared ranges³⁴ or for water³⁵ and ceramics³⁶ for radiofrequencies. The incident linearly polarized plane wave of wavelength λ_0 propagates along the axis (z -axis in Fig. 1) of the structure. We have a number of geometrical restrictions: while the radius r_i of each cylinder is independent, the height of each cylinder is set to $h_i = H/N$, where H is the height of the whole structure. Thus, for N cylinders the structure is defined by $N + 1$ param-

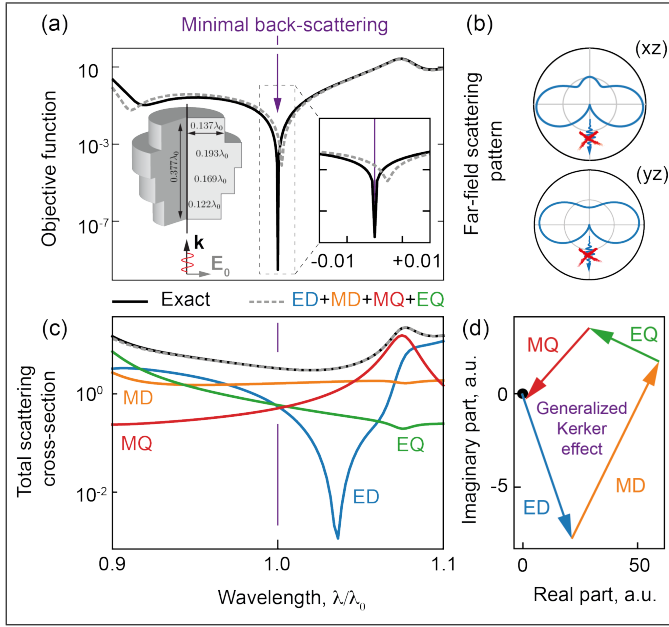


FIG. 2. Example of a scatterer with suppressed backward scattering. (a) Geometry of the scatterer and the spectrum of BCSn, showing a narrow dip at the wavelength λ_0 . The inset compares the exact BCSn value with the value calculated using multipole contributions. (b) Radiation patterns in the xz and yz planes. The patterns show forward and side radiation, with no backward radiation. (c) Total scattering cross-section and its decomposition into electric (magnetic) dipole ED (MD), electric (magnetic) quadrupole EQ (MQ) contributions. (d) Multipolar components of the backward radiating field in the complex plane. Each component is depicted as a vector, and their near-zero sum shows that the generalized Kerker condition is met.

eters. The constraints for overall geometrical dimensions of the structure are also applied:

$$r_{\min} \leq r_i \leq r_{\max}, \quad H_{\min} \leq H \leq H_{\max}, \quad (1)$$

where $r_{\min} = 1/3 \cdot \lambda_0/n$, $r_{\max} = 1.2 \cdot \lambda_0/n$, $H_{\min} = 0.4 \cdot \lambda_0/n$, $H_{\max} = 2 \cdot \lambda_0/n$. These constraints naturally limit the size parameter and the number of possible Mie resonance that can be excited in the structure by a plane wave³⁷ that simplifies the consideration and allows to identify the underlying physics beyond the observed backscattering suppression.

The backward scattered radiation can be characterized by the backward scattering cross-section (BCS) quantity

$$\sigma_{\text{bw}} = \lim_{r \rightarrow \infty} 4\pi r^2 \frac{|E_{\text{bw}}(r)|^2}{|E_0|^2}, \quad (2)$$

where E_{bw} is the amplitude of the scattered field in the far-field domain in the direction opposite to the incident wave, E_0 is the amplitude of the incident plane wave²⁹. As the objective function, we minimize the BCS at wavelength of λ_0 normalized over the minimal geometric cross section

$$\text{BCSn} = \frac{\sigma_{\text{bw}}}{\sigma_{\min}} \rightarrow \min, \quad (3)$$

where $\sigma_{\min} = \pi r_{\min}^2$. We use CMA-ES optimization algorithm, which does not require extensive hyper-parameter op-

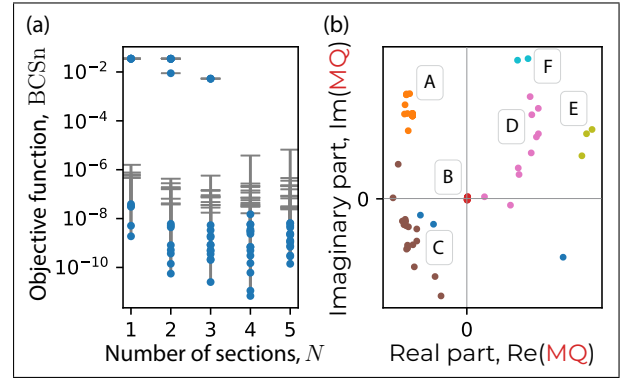


FIG. 3. (a) BCSn values for all found solutions with near-zero backscattering. (b) Contribution of magnetic quadrupole (MQ) to the backward scattering field for all found solutions, represented in the complex plane. Dots with the same color represent solution within the same cluster, each cluster marked by a number. Blue-colored dots are noisy samples and not included in any cluster.

timization and suits for black-box optimization, when no preliminary information about the fitness function behavior is provided, as in our case. More details on the algorithm is provided in Supplementary Materials Sec. 1, while the details on simulation method are presented in Supplementary Materials Sec. 2.

One of the found examples of scatterers with minimal BCSn is shown in the inset of Fig. 2 (a). The far-field scattering pattern of this structure in (xz)- and (yz)-planes are depicted in Fig. 2 (b) showing dominant forward and sideways scattering while the BCSn is close to zero. The spectrum of BCSn is presented in Fig. 2 (a) with a sharp minimum at the wavelength of λ_0 reaching the theoretical value of 10^{-9} .

The physical mechanism beyond the observed BCSn suppression can be clarified with help of the multipole theory which is a powerful tool in electromagnetics^{3,38-41} and nanophotonics^{6,42-44}. Here, we will work in the basis of Cartesian multipoles for simplicity^{45,46}. Due to the size restrictions of our geometry, there are dominant contributions of the first multipoles up to magnetic and electric quadrupoles only. Indeed, the scattering spectrum in Fig. 2 (c) shows partial cross sections correspondent to $x(y)$ -components of electric (magnetic) dipoles, and $xy(yz)$ -components of the electric (magnetic) quadrupoles which being summed give the total scattering cross section with high accuracy. The other components of dipoles and quadrupoles are not excited due to the symmetry of the problem. Thus, the backward scattering field can be expanded in terms of the named multipoles^{6,29}

$$E_{\text{bw}} = \frac{k^2}{4\pi\epsilon_0} \frac{e^{ikr}}{r} \left(\underbrace{p_x}_{\text{ED}} + \underbrace{\frac{m_y}{c}}_{\text{MD}} - i \underbrace{\frac{k}{6} Q_{xy}}_{\text{EQ}} - i \underbrace{\frac{k}{6c} M_{yz}}_{\text{MQ}} + \dots \right), \quad (4)$$

where the multipolar moments are computed in accordance with Ref.⁴⁷. The real and imaginary parts of multipole field components in Eq. (4) at the wavelength λ_0 are shown in Fig. 2 (d) with arrows in a complex plane representing electric

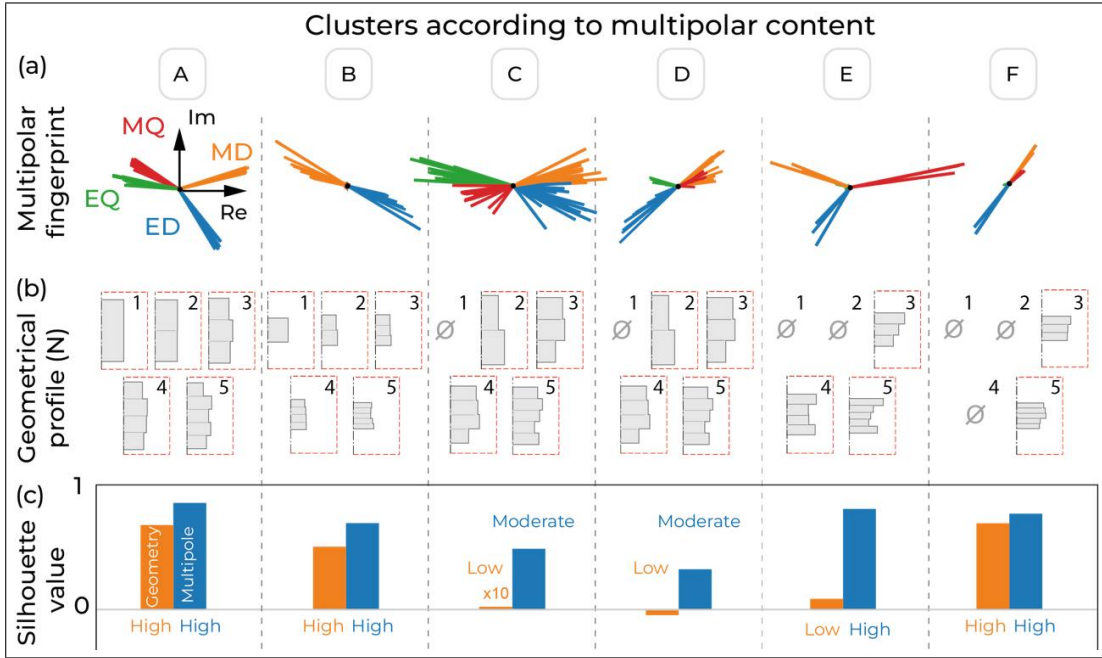


FIG. 4. Results of clustering analysis. Each row in the table corresponds to a single cluster, identified by a number. Column (a): multipolar contributions of all solutions within each cluster, represented in the complex plane. Column (b): examples of structures within each cluster for specific numbers of sections, ranging from $N = 1$ to $N = 5$. Column (c): Silhouette values (S_v) for each cluster, calculated using Euclidean distance in the space of multipolar contributions (Multipole) and the distance in the space of geometries (Geometry), as defined by (6). Low, moderate, and high are related to cohesion of the cluster in the corresponding space.

dipole (ED), magnetic dipole (MD), electric quadrupole (EQ), and magnetic quadrupole (MQ) components. One should note that the sum of these arrows appears to be close to zero that corresponds to the so-called generalized Kerker condition^{6,28,29}. Compared to the standard Kerker effect where only the sum of dipole components cancel each other, here all four components contribute to zero backscattering. At the same time, it is not exact zero, although it explains the origin of the appeared BCSn suppression. Fig. 2 (a) shows that the BCSn computed with the four multipoles only has minimum near the target wavelength λ_0 , however neither its value nor the exact spectral position do not coincide with the numerically obtained ones. In order to get the exact matching, one should consider contribution of higher order multipoles, which may be unreasonable for the proposed physical interpretation.

Next, we addressed the connection between the number of sections in the structure and the obtained minimal value of BCSn. Increasing the number of sections, one increases the degrees of freedom in scatterer's geometry. Fig. 3 (a) shows BCSn for all found minimal solutions depending on the number of sections N . To our surprise, increasing the number of layers does not significantly decrease minimum value of BCSn despite the growth of the optimization parameters number. The typical minimal BCSn values do not drop below the value of 10^{-9} for the considered values of N . The near-zero BCSn values are unstable and change dramatically even for small parameter perturbations. This instability is illustrated with the error bars. More details on error calculation is provided are Supplementary Materials Sec. 3. The reason to this

instability and large error margins is related to numerical values of drastically different scales, when near-zero BCSn is computed.

Finally, we would like to turn to classification of the found scatterers according to their multipolar content. We visualized all found optimal solutions in Fig. 3 (b) in a complex plane defining magnetic quadrupole (MQ) contribution in backward radiating field

$$MQ = -i \frac{k}{6c} M_{yz}. \quad (5)$$

Here we need to note that the imaginary part of quadrupole field components and related partial extinction cross-sections can have arbitrary sign as the optical theorem does not put any restrictions on the sign of partial cross-sections in the case of non-orthogonal channels^{48,49}. We have applied DBSCAN clustering algorithm from `scikit-learn` Python library^{50,51} to analyze the obtained datasets with all four dipole and quadrupole contributions according to Eq. (4). The found different clusters are shown with colours in Fig. 3 (b). Details on clustering parameters are presented in Supplementary Materials Sec. 4.

The obtained clusters are visualized according to their multipolar content in the first row of Fig. 4. Colored arrows correspond to complex field amplitude for different multipoles. Each cluster contains many solutions with relatively close multipolar content and, therefore, radiation pattern. Radiation patterns for each cluster are shown in Supplementary Materials Sec. 4. We need to stress that the found multipolar clusters form different types of generalized Kerker regimes which can

be hardly predicted by means of any rigorous theory. Only the class B corresponds to standard dipole Kerker regime. However it is hard to conclude whether the obtained classes can be found for different geometries and morphology of scatterers.

Each column in Fig. 4 (b) represents examples of optimized structures for specific number of sections from $N = 1$ to $N = 5$. One can notice that some clusters do not include structures with all values of N . For instance, cylindrical structures $N = 1$ enter only cluster A–B, and structures with $N = 2$ enter clusters A–C, while structures with $N = 5$ enter all clusters. That supports an intuitive conclusion that the larger is the parameter space the larger number of clusters can be formed.

It is an intriguing question how the geometrical form and multipolar content (far-field scattering pattern) are connected. To answer it, we have performed analysis of the “distance” between different species in the parametric space of their multipolar content and the distance in geometrical space using silhouette score S_v ⁵² (see Supplementary Materials Sec. 4). For the multipolar components, we utilized Euclidean distance in 8–dimensional space of the real and imaginary parts of complex components. For the geometries, we define a distance between two scatterers as follows

$$d(i, j) = \int_{-\max(H_1, H_2)/2}^{\max(H_1, H_2)/2} |r_i(z) - r_j(z)| dz, \quad (6)$$

where $r_i(z)$ is a shape curve defining the scatterer as a solid of revolution, centered at the geometrical center of the scatterer. This induced distance compares the 2D shape of the geometric silhouettes of the structures shown in Fig. 4 (b). The obtained values are shown in Fig. 4 (c). The closer is S_v to 1, the smaller is the cluster distribution. One can see that while each cluster contains species with relatively close multipolar content ($S_v \geq 0.5$), the geometrical S_v can be close to zero for some clusters (C, D, E). That basically means that each cluster contains examples of scatterers which have very close multipolar content but significantly different geometrical shape. This is another example proving that free-form geometry optimization of photonic structures is an ill-posed and ambiguous problem.

We have demonstrated the inverse design of metaatoms based on dielectric Mie resonators with cylindrical symmetry using the CMAES algorithm. The algorithm effectively identified resonator architectures made up of any number of sections that exhibit zero backscattering. The predicted backscattering efficiency can be as low as 10^{-9} of geometrical cross-section. Tailoring the optical response of the resonator based on its architecture is, in principle, a multi-solution problem. Clustering the solutions according to the multipolar content reveals that there exist several classes satisfying generalized Kerker condition. Each class contains structures with the same multipolar content and far-field radiation pattern but various geometry. Thus, one can conclude that the multipolar expansion is a powerful tool for inverse design of nanophotonic structures with pre-designed optical properties.

ACKNOWLEDGMENTS

We thank Pavel Ginzburg and Andrey Bogdanov for the discussions. The work of A.K. was financially supported by the ITMO Fellowship Program. The work was supported by the Federal Academic Leadership Program Priority 2030.

DATA AVAILABILITY STATEMENT

The data that support the findings of this study are available from the corresponding author upon reasonable request.

- ¹Y. Kivshar, “The rise of mie-tronics,” (2022).
- ²G.-X. Liu, J.-F. Liu, W.-J. Zhou, L.-Y. Li, C.-L. You, C.-W. Qiu, and L. Wu, “Inverse design in quantum nanophotonics: combining local-density-of-states and deep learning,” *Nanophotonics* **12**, 1943–1955 (2023).
- ³M. Poleva, K. Frizyuk, K. Baryshnikova, A. Evlyukhin, M. Petrov, and A. Bogdanov, “Multipolar theory of bianisotropic response of meta-atoms,” *Physical Review B* **107**, L041304 (2023).
- ⁴R. Alaei, M. Albooyeh, A. Rahimzadegan, M. S. Mirmoosa, Y. S. Kivshar, and C. Rockstuhl, “All-dielectric reciprocal bianisotropic nanoparticles,” *Physical Review B - Condensed Matter and Materials Physics* **92** (2015), 10.1103/PhysRevB.92.245130, arXiv: 1508.06965.
- ⁵P. D. Terekhov, K. V. Baryshnikova, Y. A. Artyemyev, A. Karabchevsky, A. S. Shalin, and A. B. Evlyukhin, “Multipolar response of nonspherical silicon nanoparticles in the visible and near-infrared spectral ranges,” *Physical Review B* **96**, 1–8 (2017).
- ⁶A. V. Kuznetsov, A. Canós Valero, H. K. Shamkhi, P. Terekhov, X. Ni, V. Bobrov, M. V. Rybin, and A. S. Shalin, “Special scattering regimes for conical all-dielectric nanoparticles,” *Sci. Rep.* **12**, 1–19 (2022).
- ⁷A. Canós Valero, H. K. Shamkhi, A. S. Kupriianov, T. Weiss, A. A. Pavlov, D. Redka, V. Bobrov, Y. Kivshar, and A. S. Shalin, “Superscattering emerging from the physics of bound states in the continuum,” *Nat. Commun.* **14**, 1–13 (2023).
- ⁸N. Wang, W. Yan, Y. Qu, S. Ma, S. Z. Li, and M. Qiu, “Intelligent designs in nanophotonics: from optimization towards inverse creation,” *Photonix* **2**, 1–35 (2021).
- ⁹L. Ohnoutek, J.-Y. Kim, J. Lu, B. J. Olohan, D. M. Rășădean, G. Dan Pantoș, N. A. Kotov, and V. K. Valev, “Third-harmonic mie scattering from semiconductor nanohelices,” *Nature Photonics* **16**, 126–133 (2022).
- ¹⁰S. Molesky, Z. Lin, A. Y. Piggott, W. Jin, J. Vucković, and A. W. Rodriguez, “Inverse design in nanophotonics,” *Nature Photonics* **12**, 659–670 (2018), publisher: Springer US.
- ¹¹E. Bayati, R. Pestourie, S. Colburn, Z. Lin, S. G. Johnson, and A. Majumdar, “Inverse Designed Metalenses with Extended Depth of Focus,” *ACS Photonics* **7**, 873–878 (2020), arXiv: 1910.06542.
- ¹²A. Estrada-Real, A. Khairreh-Walieh, B. Urbaszek, and P. R. Wiecha, “Inverse design with flexible design targets via deep learning: Tailoring of electric and magnetic multipole scattering from nano-spheres,” *Photonics and Nanostructures-Fundamentals and Applications* **52**, 101066 (2022).
- ¹³S. So, T. Badloe, J. Noh, J. Bravo-Abad, and J. Rho, “Deep learning enabled inverse design in nanophotonics,” *Nanophotonics* **9**, 1041–1057 (2020).
- ¹⁴P. R. Wiecha and O. L. Muskens, “Deep learning meets nanophotonics: a generalized accurate predictor for near fields and far fields of arbitrary 3d nanostructures,” *Nano letters* **20**, 329–338 (2019).
- ¹⁵S. Krasikov, A. Tranter, A. Bogdanov, and Y. Kivshar, “Intelligent nanophotonics empowered by machine learning,” *OEA* **5**, 210147–1–210147–24 (2022).
- ¹⁶S. So, J. Mun, and J. Rho, “Simultaneous inverse design of materials and structures via deep learning: demonstration of dipole resonance engineering using core-shell nanoparticles,” *ACS applied materials & interfaces* **11**, 24264–24268 (2019).
- ¹⁷Z. A. Kudyshev, A. V. Kildishev, V. M. Shalaev, and A. Boltasseva, “Machine-learning-assisted metasurface design for high-efficiency thermal emitter optimization,” *Appl. Phys. Rev.* **7** (2020), 10.1063/1.5134792.

- ¹⁸W. Li, H. Barati Sedeh, D. Tsvetkov, W. J. Padilla, S. Ren, J. Malof, and N. M. Litchinitser, "Machine Learning for Engineering Meta-Atoms with Tailored Multipolar Resonances," *Laser & Photonics Reviews* **18**, 2300855 (2024).
- ¹⁹Y. Augenstein, T. Repán, and C. Rockstuhl, "Neural Operator-Based Surrogate Solver for Free-Form Electromagnetic Inverse Design," *ACS Photonics* **10**, 1547–1557 (2023).
- ²⁰S. An, B. Zheng, M. Y. Shalaginov, H. Tang, H. Li, L. Zhou, J. Ding, A. M. Agarwal, A. M. Agarwal, C. Rivero-Baleine, M. Kang, K. A. Richardson, T. Gu, J. Hu, C. Fowler, C. Fowler, H. Zhang, and H. Zhang, "Deep learning modeling approach for metasurfaces with high degrees of freedom," *Opt. Express* **28**, 31932–31942 (2020).
- ²¹P. R. Wiecha, "Deep learning for nano-photonic materials—the solution to everything!?" *Current Opinion in Solid State and Materials Science* **28**, 101129 (2024).
- ²²I. Volkov, S. Mitsai, S. Zhogolev, D. Kornovan, A. Sheremet, R. Savelev, and M. Petrov, "Non-radiative configurations of a few quantum emitters ensembles: Evolutionary optimization approach," *Applied Physics Letters* **124**, 084001 (2024).
- ²³P. R. Wiecha, A. Arbouet, C. Girard, A. Lecestre, G. Larrieu, and V. Paillard, "Evolutionary multi-objective optimization of colour pixels based on dielectric nanoantennas," *Nat. Nanotechnol.* **12**, 163–169 (2017).
- ²⁴P. R. Wiecha, P. R. Wiecha, C. Majorel, C. Girard, A. Cuche, V. Paillard, O. L. Muskens, and A. Arbouet, "Design of plasmonic directional antennas via evolutionary optimization," *Opt. Express* **27**, 29069–29081 (2019).
- ²⁵R. Hamano, S. Saito, M. Nomura, and S. Shirakawa, "Cma-es with margin: Lower-bounding marginal probability for mixed-integer black-box optimization," in *Proceedings of the genetic and evolutionary computation conference* (2022) pp. 639–647.
- ²⁶M. Nomura, Y. Akimoto, and I. Ono, "Cma-es with learning rate adaptation: Can cma-es with default population size solve multimodal and noisy problems?" in *Proceedings of the Genetic and Evolutionary Computation Conference* (2023) pp. 839–847.
- ²⁷M. Kerker, D.-S. Wang, and C. L. Giles, "Electromagnetic scattering by magnetic spheres," *Journal of the Optical Society of America* **73**, 765–765 (1983), ISBN: 1936-0851.
- ²⁸W. Liu and Y. S. Kivshar, "Generalized Kerker effects in nanophotonics and meta-optics [Invited]," *Opt. Express* **26**, 13085–13105 (2018).
- ²⁹R. Alaee, R. Filter, D. Lehr, F. Lederer, and C. Rockstuhl, "A generalized Kerker condition for highly directive nanoantennas," *Opt. Lett.* **40**, 2645–2648 (2015).
- ³⁰D. Dobrykh, D. Shakirova, S. Krasikov, A. Mikhailovskaya, I. Yusupov, A. Slobozhanyuk, K. Ladutenko, D. Filonov, A. Bogdanov, and P. Ginzburg, "Multipole engineering for enhanced backscattering modulation," *Phys. Rev. B* **102**, 195129 (2020).
- ³¹K. V. Baryshnikova, M. I. Petrov, V. E. Babicheva, and P. A. Belov, "Plasmonic and silicon spherical nanoparticle anti-reflective coatings," *Scientific reports* **6**, 1 (2016).
- ³²V. Babicheva, M. Petrov, K. Baryshnikova, and P. Belov, "Reflection compensation mediated by electric and magnetic resonances of all-dielectric metasurfaces [Invited]," *Journal of the Optical Society of America B* **34**, 18–28 (2017), arXiv: 1511.08473.
- ³³M. M. Bukharin, V. Ya. Pecherkin, A. K. Ospanova, V. B. Il'in, L. M. Vasilyak, A. A. Basharin, and B. Luk'yanchuk, "Transverse Kerker effect in all-dielectric spheroidal particles," *Sci. Rep.* **12**, 1–12 (2022).
- ³⁴D. E. Aspnes and A. A. Studna, "Dielectric functions and optical parameters of Si, Ge, GaP, GaAs, GaSb, InP, InAs, and InSb from 1.5 to 6.0 eV," *Phys. Rev. B* **27**, 985–1009 (1983).
- ³⁵U. Kaatzte, "Complex permittivity of water as a function of frequency and temperature," *J. Chem. Eng. Data* **34**, 371–374 (1989).
- ³⁶H. K. Shamkhi, K. V. Baryshnikova, A. Sayanskiy, P. Kapitanova, P. D. Terekhov, P. Belov, A. Karabchevsky, A. B. Evlyukhin, Y. Kivshar, and A. S. Shalin, "Transverse Scattering and Generalized Kerker Effects in All-Dielectric Mie-Resonant Metaoptics," *Phys. Rev. Lett.* **122**, 193905 (2019).
- ³⁷A. I. Kuznetsov, A. E. Miroshnichenko, M. L. Brongersma, Y. S. Kivshar, and B. Luk'yanchuk, "Optically resonant dielectric nanostructures," *Science* **354** (2016), 10.1126/science.aag2472.
- ³⁸R. Raab and O. De Lange, *Multipole Theory in Electromagnetism: Classical, Quantum and Symmetry Aspects, with Applications* (Oxford Science Publications, Oxford, 2005) iSSN: 0305-4470.
- ³⁹K. Frizyuk, I. Volkovskaya, D. Smirnova, A. Poddubny, and M. Petrov, "Second-harmonic generation in Mie-resonant dielectric nanoparticles made of noncentrosymmetric materials," *Phys. Rev. B* **99**, 075425 (2019).
- ⁴⁰S. Gladyshev, K. Frizyuk, and A. Bogdanov, "Symmetry analysis and multipole classification of eigenmodes in electromagnetic resonators for engineering their optical properties," *Phys. Rev. B* **102**, 075103 (2020).
- ⁴¹Z. Sadrieva, K. Frizyuk, M. Petrov, Y. Kivshar, and A. Bogdanov, "Multipolar origin of bound states in the continuum," *Phys. Rev. B* **100**, 115303 (2019).
- ⁴²T. Liu, R. Xu, P. Yu, Z. Wang, and J. Takahara, "Multipole and multi-mode engineering in Mie resonance-based metastructures," *Nanophotonics* **0**, 1115–1137 (2020), iSSN: 0000000236836.
- ⁴³A. E. Miroshnichenko, A. B. Evlyukhin, Y. F. Yu, R. M. Bakker, A. Chipouline, A. I. Kuznetsov, B. Luk'yanchuk, B. N. Chichkov, and Y. S. Kivshar, "Nonradiating anapole modes in dielectric nanoparticles," *Nat. Commun.* **6**, 1–8 (2015).
- ⁴⁴A. B. Evlyukhin, C. Reinhardt, and B. N. Chichkov, "Multipole light scattering by nonspherical nanoparticles in the discrete dipole approximation," *Phys. Rev. B* **84**, 235429 (2011).
- ⁴⁵A. B. Evlyukhin, T. Fischer, C. Reinhardt, and B. N. Chichkov, "Optical theorem and multipole scattering of light by arbitrarily shaped nanoparticles," *Phys. Rev. B* **94**, 205434 (2016).
- ⁴⁶J. Mun, S. So, J. Jang, and J. Rho, "Describing Meta-Atoms Using the Exact Higher-Order Polarizability Tensors," *ACS Photonics* **7**, 1153–1162 (2020).
- ⁴⁷R. Alaee, C. Rockstuhl, and I. Fernandez-Corbaton, "An electromagnetic multipole expansion beyond the long-wavelength approximation," *Opt. Commun.* **407**, 17–21 (2018).
- ⁴⁸A. E. Miroshnichenko, A. B. Evlyukhin, Y. S. Kivshar, and B. N. Chichkov, "Substrate-induced resonant magnetoelectric effects with dielectric nanoparticles," *ACS Photonics* **2**, 1423–1428 (2015).
- ⁴⁹S. Krasikov, M. Odit, D. Dobrykh, I. Yusupov, A. Mikhailovskaya, D. Shakirova, A. Shcherbakov, A. Slobozhanyuk, P. Ginzburg, D. Filonov, and A. Bogdanov, "Multipolar Engineering of Subwavelength Dielectric Particles for Scattering Enhancement," *Physical Review Applied* **15**, 024052 (2021).
- ⁵⁰M. Ester, H. Kriegel, J. Sander, and X. Xu, "A Density-Based Algorithm for Discovering Clusters in Large Spatial Databases with Noise," *Knowledge Discovery and Data Mining* (1996).
- ⁵¹F. Pedregosa, G. Varoquaux, A. Gramfort, V. Michel, B. Thirion, O. Grisel, M. Blondel, P. Prettenhofer, R. Weiss, V. Dubourg, J. Vanderplas, A. Passos, D. Cournapeau, M. Brucher, M. Perrot, and E. Duchesnay, "Scikit-learn: Machine learning in Python," *Journal of Machine Learning Research* **12**, 2825–2830 (2011).
- ⁵²P. J. Rousseeuw, "Silhouettes: A graphical aid to the interpretation and validation of cluster analysis," *J. Comput. Appl. Math.* **20**, 53–65 (1987).

I. OPTIMIZATION ALGORITHM

The main idea of the algorithm is following: each generation (step of the algorithm) a new set of candidate solutions is created. The set is sampled in $N + 1$ – dimensional parameter space using the multidimensional normal distribution. Then the fitness function is calculated for each candidate and a new mean vector and covariance matrix are calculated based on the obtained values. The obtained mean vector and covariance matrix are used in the next generation to generate a new set of candidate structures.

We use Python-implemented CMAES library called `cmaes`¹.

Initial step-size (standard deviation) is chosen $\sigma = 1/15\lambda_0$. The termination criteria was chosen such that standard deviation in the generation for each parameter is less than $1.67 \cdot 10^{-5}\lambda_0$ or the generations number exceeds 300. Population size is different for each number of sections. The number of total runs, population sizes, and mean number of iterations are presented in Table I.

TABLE I. Parameters of the optimization.

N	Total runs	Population size	Generations mean number
1	10	10	102.2
2	15	12	110.3
3	15	14	171.5
4	15	16	199
5	15	18	236.5

II. NUMERICAL MODELING

We use the COMSOL Multiphysics® software and its wave optics module to calculate the scattering field of considered system². To drastically speed up calculations during the optimization process we use axial symmetry model with azimuthal numbers $m = -1, 1$ ³. We use spherical host domain with radius $\approx 5\lambda_0$ and perfectly matched layer with thickness $\approx 3\lambda_0$ to simulate infinite free space. The element size of the mesh is chosen to be smaller than $\lambda_0/n/30$, where n is refractive index of the meshed domain. We calculate far-field using built-in Far-Field Domain.

III. ERROR BARS

In Fig. 1 (a), the relative distance between the parameter H for each candidate at every iteration and the corresponding value H^* for the best candidate

$$\frac{|H - H^*|}{H^*} \quad (1)$$

in the final generation is shown. It is evident that the relative distance, and consequently the standard deviation (step-size), decreases with each iteration. In contrast, the relative distance

for BCSn, depicted in Fig. 1 (b), stops decreasing after a certain generation and stabilizes around a fixed value. These figures show that even small perturbations in the system parameter, and therefore small changes in the model mesh, can lead to significant variations in the BCSn value.

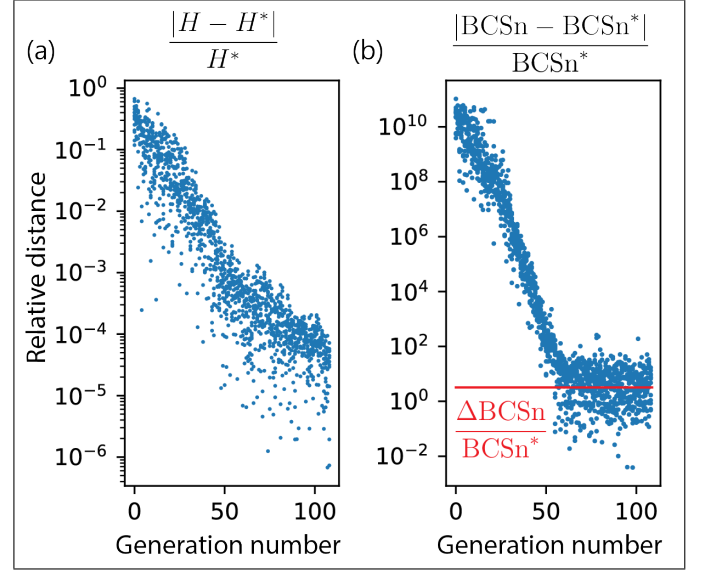


FIG. 1. Relative distances between (a) the parameter H and (b) BCSn for each candidate at every iteration and the corresponding values H^* and $BCSn^*$ for the best candidate.

The sensitivity of BCSn does not correspond to a high derivative with respect to the parameter. If it did, the relative distance of BCSn would decrease as the parameter perturbations (H) decrease. We interpret this sensitivity as indicative of a noisy fitness function landscape near very low BCSn values due to computational errors.

To find the level the dependency stops decreasing, we calculate the average value of relative distance for BCSn across all candidates over the last 10 generations. This resulting value can be expressed as:

$$\frac{\Delta BCSn}{BCSn^*}, \quad (2)$$

where $\Delta BCSn$ is absolute error of found $BCSn^*$ minimum. The $\Delta BCSn$ is depicted as error bars in Fig. 3 (a) in the main text. Minima associated with relatively high BCSn values have smaller error bars, because these BCSn values are large enough to avoid numerical issues, unlike the case with relatively small BCSn values.

IV. CLUSTERIZATION

We choose minimum number of points equal 2 and ϵ parameter for DBSCAN algorithm such that silhouette score has a maximum value⁴.

To calculate silhouette value s_i for single data point i of cluster C_k one should introduce a distance between two data

points $d(i, j)$. The average distance between i and all other data points in cluster C_k is

$$a_i = \text{mean}_{j \in C_k, j \neq i} d(i, j). \quad (3)$$

The smallest distance between i and any other cluster is

$$b_i = \min_{C_r \neq C_k} \left(\text{mean}_{j \in C_r} d(i, j) \right). \quad (4)$$

The silhouette value for single data point i is defined by

$$s_i = \frac{b_i - a_i}{\max(a_i, b_i)}. \quad (5)$$

Now we introduce silhouette value for the cluster C_k , S_v

$$S_v = \text{mean}_{i \in C_k} s_i. \quad (6)$$

One can see that $-1 \leq S_v \leq 1$. The larger value indicates better clustering and vice versa.

For clustering all minima found we use Euclidean distance between 8 features: real and imaginary parts of ED, MD, EQ, and MQ. All the features are normalized so that all of them lies in the range from -1 to 1. The mean S_v value over all the clusters of the resulting clustering is 0.59. Radiation patterns for resulting clusters are shown in Fig. 2.

¹M. Nomura and M. Shibata, "cmaes : A simple yet practical python library for cma-es," arXiv preprint arXiv:2402.01373 (2024).

²COMSOL AB, Stockholm, Sweden, "Comsol multiphysics®," .

³S. Gladyshev, O. Pashina, A. Proskurin, A. Nikolaeva, Z. Sadrieva, M. Petrov, A. Bogdanov, and K. Frizyuk, "Fast Simulation of Light Scattering and Harmonic Generation in Axially Symmetric Structures in COMSOL," ACS Photonics **11**, 404–418 (2024).

⁴P. J. Rousseeuw, "Silhouettes: A graphical aid to the interpretation and validation of cluster analysis," J. Comput. Appl. Math. **20**, 53–65 (1987).

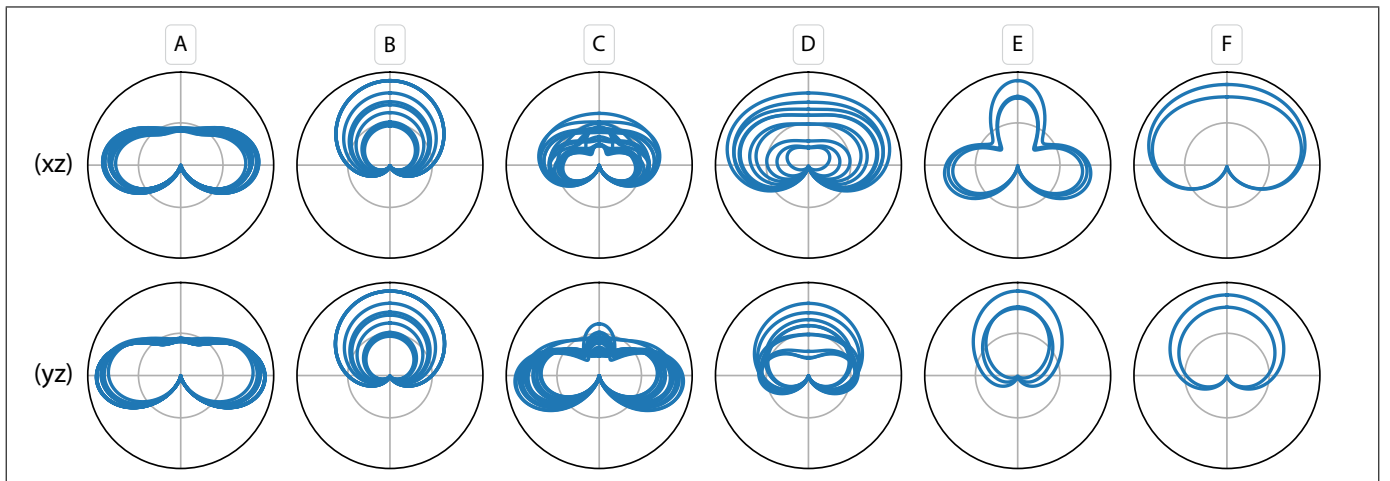


FIG. 2. Radiation patterns for found clusters in xz and yz planes.